JOURNAL OF SYNCHROTRON RADIATION

ISSN 1600-5775

The local and average structure of Ba(Ti, Ce)O_3 perovskite solid solution: effect of cerium concentration and particle size

Giorgia Confalonieri,[a]*‡ Vincenzo Buscaglia,[b] Giovanna Canu,[b] Maria Teresa Buscaglia[b] and Monica Dapiaggi[a]

[a]Dipartimento di Scienze della Terra, Università degli Studi di Milano, Milano, Italy, and [b]Istituto di Chimica della Materia Condensata e di Tecnologie per l'Energia (ICMATE), Consiglio Nazionale delle Ricerche (CNR), Genova, Italy. *Correspondence e-mail: giorgia.confalonieri@unito.it

Received 1 February 2019
Accepted 2 April 2019

Edited by A. F. Craievich, University of São Paulo, Brazil

‡ Current affiliation: Dipartimento di Scienze della Terra, Università degli Studi di Torino, Torino, Italy.

Keywords: perovskite; size effect; Pair Distribution Function.

The amazing properties of ferroelectric perovskite $BaTiO_3$ (BT) and its solid solutions make them indispensable for many technological applications (*e.g.* multilayer capacitors). Unfortunately, the so-called 'size effect' limits their use. Indeed, under a certain critical particle size, these materials show a suppression of the spontaneous polarization and thus of the ferroelectric properties. In pure nanometric $BaTiO_3$, this is related to a certain local structural disorder. However, only a few studies have explored BT solid solutions, where the doping effect, coupled to the reduced particle size, can play an important role. Therefore, in this work, the structure of $BaCe_xTi_{1-x}O_3$ (x = 0.02–0.20) was explored by traditional Rietveld method and Pair Distribution Function. Samples present a particle size from 80–160 nm to 400–1000 nm depending on increasing x. The carbox approach was applied, investigating the evolution of the local structure, its modifications and the structural coherent correlation length, as a function of cerium amount. Results demonstrate a cooperative effect of composition and reduced size in the ferroelectricity loss. The two, in fact, contribute to intensify the local structural disorder, decreasing the structural coherent correlation length. The local structural disorder is thus confirmed to be a relevant factor in the ferroelectric properties degradation.

1. Introduction

$BaTiO_3$ ferroelectric perovskites and their solid solutions are extensively employed in many technological fields. These types of oxides find wide applications as pyroelectric sensors, electromechanical transducers, multilayer capacitors and so on (Moulson & Herbert, 2003; Shrout & Zhang, 2007; Yasmm *et al.*, 2011). Unfortunately, demanding advances in nano-science and technology revealed an important limitation in their use. Indeed, the so-called 'size effect', which implicates a degradation of the ferroelectricity up to its complete disappearance, occurs under a critical grain size (around 30 nm) (Nuraje & Su, 2013). The decline of the material properties can present changes of up to 80% if compared with their bulk counterparts (Ihlefeld *et al.*, 2016) and therefore it imposes important compromises in the devices miniaturization (Alguero *et al.*, 2016). For this reason, many studies focused on the link between reduced grain size and the ferroelectricity loss. Ferroelectricity appears as a collective phenomenon, arising from the competition between short-range covalent repulsions and long-range Coulomb interactions (Cochran, 1960). It is possible that, when reducing from the bulk to the nanoscale, these interactions are modified. It is expected that physical properties of ferroelectric nano-perovskites will be

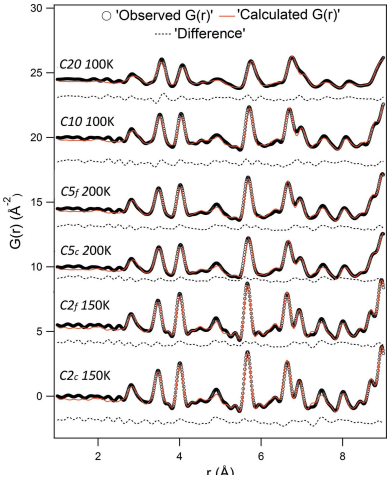

strongly affected by the electromechanical boundary conditions (*e.g.* surface charge, misfit epitaxial strain and inhomogeneous effects, particularly strain gradients) (Zhu & Liu, 2011). By a classical phenomenological thermodynamic theory (Landau Ginzburg Devonshire approach) the ferroelectric suppression can be, instead, caused by an intrinsic nature of the nanoparticles smaller than a certain critical size. The effect can be interpreted as a phase transition from a ferroelectric to a paraelectric state taking place at a critical system size (Lin *et al.*, 2006). On the other hand, a different explanation considers the impurity surface ions, structural imperfections such as oxygen vacancies, dislocations, disorder *etc*., as the causes of a local depolarization field which prevents the formation of the ferroelectric phases (Gerra *et al.*, 2006). Despite the fact that the exact origin of the size effect is still not established (Ihlefeld *et al.*, 2016), structural studies, performed on nanometric $BaTiO_3$, gave some interesting additional information. From the structural point of view, the suppression of the ferroelectric properties (under a critical size) is linked to the stabilization of the cubic structure. Being centrosymmetric, titanium displacement, which is at the basis of the spontaneous polarization onset (Müller & Berlinger, 1986; Müller *et al.*, 1987; Comès *et al.*, 1970; Miura *et al.*, 2011), is forbidden. However, this ideal perovskite structure is only an image of a more disordered local environment. Indeed, papers by Yoneda *et al.* and Page *et al.* report that cubic nanometric $BaTiO_3$ presents local tetragonal distortions correlated only over short-range distances (Yoneda *et al.*, 2013; Page *et al.*, 2010). By EXAFS (extended X-ray absorption fine structure) and XANES (X-ray absorption near-edge structure) analysis, Frenkel *et al.* find a local titanium displacement, in contrast to the cubic macroscopic crystal structures (Frenkel *et al.*, 1999). Results of Petkov *et al.* (2008) clearly show that TiO_6 octahedra are always distorted in submicrometre- and nanometric-sized samples. The material maintains its tetragonal-type lattice atomic ordering within at least three unit cells. This distortion (*i.e.* the increased displacement in the centres of the positive and negative charges) should result in an enhancement of their local dipole moment, but this is not translated on average into an enhancement of the net spontaneous polarization (Petkov *et al.*, 2008). Increased distortions were detected while decreasing the particle size, albeit in conjunction with a tendency to a cubic average structure (Smith *et al.*, 2008). In general, the reduced size provokes deep local distortions, with the structures losing their long-range order, reducing the length of structural coherence and resulting in an average deterioration of the spontaneous polarization (Petkov *et al.*, 2008). The local structure is a key point to better understand the 'size effect' on ferroelectric perovskites.

In this paper, the case of $BaCe_xTi_{1-x}O_3$ (BCT) with a reduced particle size (from 80–160 nm to 400–1000 nm depending on x) is considered. This perovskite, in its micrometric form, presents, as a function of cerium amount, a polar behaviour variation from conventional ferroelectric to relaxor via diffuse phase transition (DPT) (Shvartsman & Lupascu, 2012; Curecheriu *et al.*, 2013, 2016; Canu *et al.*, 2018). Conventional ferroelectric phase transitions of pure $BaTiO_3$ are recognized up to $x < 0.09$. Upon cooling, cubic structure transforms into tetragonal, then symmetry changes to orthorhombic and rhombohedral. At larger x, a single cubic/rhombohedral phase transition is observed until the system exhibits a clear relaxor behaviour for $x \geq 0.20$, with the stabilization of an average cubic structure at all of the temperatures (Canu *et al.*, 2018). The effect of cerium introduction thus strongly influences the ferroelectric properties as well as the average and, especially, the local structure (Confalonieri *et al.*, 2018; Canu *et al.*, 2018). In the present work, BCT samples, with the same compositions reported by Canu and co-workers and Confalonieri and co-workers, were synthesized with a reduced particle size, in order to specifically evaluate the effects of the reduced size and its coupling with cerium introduction. The Rietveld method and Pair Distribution Function (PDF) (Egami & Billinge, 2012; Billinge & Kanatzidis, 2004) are used to investigate both the average and local structure.

2. Experimental

2.1. Sample preparation

BCT powders with x = 0.02, 0.05, 0.10 and 0.20 were prepared by solid-state reaction using electronic-grade nanocrystalline precursors. Stoichiometric amounts of TiO_2 (Aeroxide P25, S_{BET} = 55.1 $m^2\ g^{-1}$; Evonik Degussa, Hanau, Germany), CeO_2 (VP AdNano Ceria 50, S_{BET} = 80.5 $m^2\ g^{-1}$, Evonik Degussa, Hanau, Germany) and $BaCO_3$ (S_{BET} = 27.6 $m^2\ g^{-1}$, Solvay Bario e Derivati, Massa, Italy) powders were wet mixed in aqueous suspension for 24 h using polyethylene jars and zirconia media. After freeze-drying, the mixtures were calcined in air for 4 h at specific temperatures depending on composition. The use of nano-sized reactants with high specific surface area (S_{BET}) enhances the reactivity and favours the compositional homogeneity of the final particles. The absence of unreacted precursors in the final products was verified by conventional X-ray diffraction (Panalytical CubiX). Compositions x = 0.02 and 0.05 were treated at two different temperatures in order to vary the particle size. The samples will be named CN with $N = 100x$. A suffix f (fine) or c (coarse) is added as a subscript when two samples of the same composition but different particle size exist. The particle sizes of the final powders were evaluated using a scanning electron microscope (LEO 1450VP) and are reported in Table 1. A size range is given to take into account the particle size dispersion.

2.2. XRPD data collection

Data collections were performed at ID22, the high-resolution beamline (Fitch, 2004) at ESRF (European Synchrotron Radiation Facility, Grenoble France). In both experiments, samples were ground and placed in borosilicate glass capillaries (0.6 mm diameter). They were measured as a function of temperature using the Oxford Cryosystems Cryostream cold nitrogen-gas blower. Conventional diffraction intensities were collected with a λ value of 0.335014 Å by a multianalyser

Table 1
Investigated samples, their composition and grain size, temperature of thermal treatment used during the synthesis and the data collection temperatures.

Set	Composition	Particle size (nm)	Thermal treatment temperature (K)	Collection temperature (K)
$C2_f$	Ba $Ce_{0.02}Ti_{0.98}O_3$	80–160	1273 (1000°C)	150, 270, 350, 450
$C2_c$	Ba $Ce_{0.02}Ti_{0.98}O_3$	350–700	1723 (1450°C)	150, 270, 350, 450
$C5_f$	Ba $Ce_{0.05}Ti_{0.95}O_3$	150–400	1373 (1100°C)	200, 300, 350, 380, 420
$C5_c$	Ba $Ce_{0.05}Ti_{0.95}O_3$	700–1200	1723 (1450°C)	200, 300, 350, 380, 420
C10	Ba $Ce_{0.10}Ti_{0.90}O_3$	250–600	1523 (1250°C)	100, 200, 300, 400
C20	Ba $Ce_{0.20}Ti_{0.80}O_3$	400–1000	1673 (1400°C)	100, 200, 300, 400

detector obtaining high-resolution data (experiment MA3151). The high-resolution mode is necessary in order to reduce the instrumental contribution to peak broadening, which is quite severe, due to the reduced size of the samples; in this way, it is possible to detect the presence of very subtle phase transitions. Each collection lasted 30 min. Total scattering intensities were collected by a flat-panel Perkin Elmer XRD 1611CP3 with an appropriate distance from the sample and a short wavelength (0.1549723 Å) reaching an experimental Qmax = 27 (experiment MA2497). Sixty images (exposure time 25 s) for each sample were recorded and then averaged and integrated. For both experiments, standard materials were measured: Si (NIST SRM 640c) and LaB_6 (NIST SRM 660c). In the second, an empty glass capillary was also collected. This latter allowed instrumental and environmental background signal to be subtracted from the data, obtaining suitable PDFs. Table 1 reports samples and collecting temperature conditions.

2.3. Data treatment

Maud software (Lutterotti *et al.*, 1999) was used to analyse the diffraction data. Structural parameters were refined according to the related space group rules; Ti and Ce were constrained in the same position and linked by fixed fractional occupancies, corresponding to the nominal composition (the occupancies were refined in the last step of the refinement, in order to check for reliability, giving the expected value within 1σ). In addition, isotropic thermal parameters, crystallite size and r.m.s microstrain (using the isotropic model) were evaluated. In order to determine correctly the latter two quantities, the instrumental contribution of the diffraction equipment was measured collecting (with the same conditions used for the samples) and refining Si (NIST SRM 640c) standard material.

PDFs were obtained normalizing and treating total scattering data by *PDFgetX3* software (Juhás *et al.*, 2013). Qmax was fixed at 26, the background was subtracted and the scale value was set at 1. The meaning of these parameters is reported elsewhere (Juhás *et al.*, 2013; Confalonieri *et al.*, 2015). In order to reduce noise in the low r region, $r$poly was assigned a value of 1.4. Local structural analyses were performed using *PDFgui* (Farrow *et al.*, 2007) software. The Qdamp parameter, obtained analyzing standard material, was fixed at 0.008.

3. Results and discussion

3.1. Rietveld refinements and average structure

Crystal systems (space groups) of BCTs were determined as a function of cerium concentration, temperature and particle size (Table 2). Refinements were performed testing the four space groups ($Pm\bar{3}m$, $P4mm$, $Amm2$, $R3m$), which occur in phase transitions of $BaTiO_3$ (Kwei *et al.*, 1993) and found also for micrometric BCTs (Confalonieri *et al.*, 2018). Goodness-of-fit parameters (Rw values) were compared to choose among the different possible polymorphs. In Fig. 1, a visual evaluation of the structural transitions can be made observing the splitting of the (220) cubic reflection. Sets $C2_c$ and $C2_f$ maintain the typical transition sequence of pure $BaTiO_3$. The paraelectric cubic structure, upon cooling, changes to tetragonal, orthorhombic and then to the rhombohedral crystal system, which are all ferroelectric structures. The same occurs in $C5_c$, but for the sample $C5_f$ the reduced size induces the stabilization of the cubic structure at all temperatures. As for the latter, the crystal system for C10 and C20 is cubic at all temperatures.

Table 2 presents the results obtained in this work compared with those of dense (relative density $\geq$ 97%) micrometric ceramics (denoted as CN_m) published elsewhere (Canu *et al.*, 2018). The average grain size of the ceramic samples gradually increases from 1 to 5 µm while increasing x from 0.02 to 0.20. The different interface boundary conditions (particles or ceramics) and the size both have an effect on the crystal structure. In fact, as already evident from Fig. 1, for the fine powder $C5_f$ the reduction of particle size alters the phase stability, stabilizing the cubic phase at lower temperatures in comparison with the coarse powder $C5_c$ and the micrometric ceramic (Table 2). Stabilization of the cubic phase over the rhombohedral phase of ceramic is observed for powder C10. As a general tendency, the unit-cell volume for compositions x = 0.02 to 0.10 increases from powders to ceramics (Table 3). Cell volumes also increase with increasing cerium amount and temperature as already observed in micrometric ceramics (Canu *et al.*, 2018). The spontaneous polarization in $BaTiO_3$ and in its solid solutions, with homovalent substitution at the B site, originates from Ti displacement (Miura *et al.*, 2011). Thus, the estimation of this parameter is essential to evaluate the material properties. The B cations position (Ti and Ce were constrained to occupy the same position, with an occupancy corresponding to the nominal chemical composition) was refined according to space groups rules. In $R3m$, Ti/Ce moves in (x x x), in (1/2 0 z) for $Amm2$ and in (1/2 1/2 z) for $P4mm$. In the cubic phase, instead, Ti and Ce sit in special position $m\bar{3}m$ and they cannot move. Displacements of the B site (δ_B) are calculated from the centre of the unit cells and their values have to be intended as collective Ti and Ce displacements. However, differently from titanium, Ce cations are expected not to shift off the centre of the octahedron, owing to their

Table 2
Space groups at different temperatures for powders and micrometric ceramics (Canu *et al.*, 2018) of the same composition.

Sample	Fine powder	Coarse powder	Micrometric ceramic	Sample	Powder	Micrometric ceramics
x = 0.02				x = 0.10		
150 K	*R*3*m*	*R*3*m*	*R*3*m*	100 K	$Pm\bar{3}m$	*R*3*m*
270 K	*Amm*2	*Amm*2	*Amm*2†	200 K	$Pm\bar{3}m$	*R*3*m*
350 K	*P*4*mm*	*P*4*mm*	*P*4*mm*	300 K	$Pm\bar{3}m$	*R*3*m*
450 K	$Pm\bar{3}m$	$Pm\bar{3}m$	$Pm\bar{3}m$	400 K	$Pm\bar{3}m$	$Pm\bar{3}m$
x = 0.05				x = 0.20		
200 K	$Pm\bar{3}m$	*R*3*m*	*R*3*m*	100 K	$Pm\bar{3}m$	*R*3*m*
300 K	$Pm\bar{3}m$	*Amm*2	*Amm*2†	200 K	$Pm\bar{3}m$	$Pm\bar{3}m$
350 K	$Pm\bar{3}m$	*P*4*mm*	*P*4*mm*†	300 K	$Pm\bar{3}m$	$Pm\bar{3}m$
380 K	$Pm\bar{3}m$	$Pm\bar{3}m$	$Pm\bar{3}m$	400 K	$Pm\bar{3}m$	$Pm\bar{3}m$
420 K	$Pm\bar{3}m$	$Pm\bar{3}m$	$Pm\bar{3}m$			

† Biphasic samples, only the predominant phase (which is in any case >97–98 wt%) is reported.

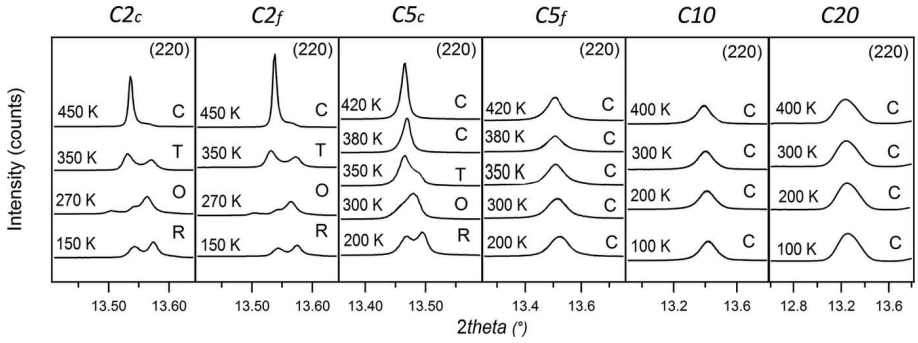

Figure 1
Evolution of the cubic reflection (220) as a function of cerium amount and temperature. Crystal systems for each sample and temperature are also reported: cubic (C), tetragonal (T), orthorhombic (O) and rhombohedral (R).

large ionic radii (0.87 versus 0.605 Å). The values of δ_B for powders and ceramics (Confalonieri *et al.*, 2018) are given in Table 3. As shown there, the combined effect of particle size and cerium incorporation reduces B displacements up to their complete suppression, as occurs in $C5_f$, C10 and C20 powders.

In micrometric $BaCe_xTi_{1-x}O_3$ ceramics, the progressive suppression of the spontaneous polarization with x and the cubic phase stabilization was proved to be related to the disruption of the correlated Ti displacements engendered by the large Ce^{4+} incorporated at the B site. Furthermore, the introduction of much larger cerium ions produces local deformation of the BO_6 octahedra and strain (Confalonieri *et al.*, 2018) which further weakens the titanium displacements correlation and, consequently, the spontaneous polarization. This strain is partially released by the creation of volume defects (*i.e.* dislocation) and local structural disorder (*i.e.* a broad distribution of the B—O bond distances). Referring to the average structure, the strain can be estimated refining the r.m.s microstrain (as explained in the *Experimental* section). However, one should consider that there are many factors that can contribute to this parameter [*e.g.* dislocations, stacking faults, local disorder, *etc.* (Balzar *et al.*, 2004)] and therefore the meaning of the microstrain should not be intended too narrowly. Fig. 2 shows a comparison of this parameter in BCT samples with different particle/grain sizes. In general, powder sets (in particular C20, C10 and $C5_f$) display higher values, due to the combined contribution coming from the reduced size and large x. It is also interesting to observe that there is a clear positive correlation, in the powder samples, between the amount of cerium and the r.m.s. microstrain. Moreover, sets with higher x are those in which the cubic polymorph is stable at all temperatures. This confirms the importance of disorder and strain in the stabilization of the cubic phase and the resulting suppression of ferroelectricity. The effects of the

Table 3
Cell volume (V) and B cations displacement, obtained by Rietveld method, for powders and micrometric ceramics (Canu *et al.*, 2018; Confalonieri *et al.*, 2018) of the same composition.

	V (Å^3)			B site displacement (Å)				V (Å^3)		B site displacement (Å)	
Sample	Fine powder	Coarse powder	Micrometric ceramic	Fine powder	Coarse powder	Micrometric ceramic	Sample	Powder	Micrometric ceramic	Powder	Micrometric ceramic
x = 0.02							x = 0.10				
150 K	64.660 (7)	64.640 (5)	64.657 (1)	0.062 (3)	0.065 (1)	0.066 (1)	100 K	66.268 (9)	66.359 (2)	0	0.039 (8)
270 K	64.753 (9)	64.738 (8)	64.760 (1)	0.057 (1)	0.057 (1)	Und.†	200 K	66.383 (3)	66.483 (1)	0	0.028 (1)
350 K	64.873 (2)	64.854 (6)	64.872 (7)	0.061 (1)	0.052 (6)	0.040 (2)	300 K	66.522 (3)	66.626 (1)	0	0.042 (3)
450 K	64.971 (1)	64.985 (7)	64.998 (2)	0	0	0	400 K	66.650 (1)	66.761 (3)	0	0
x = 0.05							x = 0.20				
200 K	65.201 (1)	65.350 (9)	65.377 (1)	0	0.035 (1)	0.050 (1)	100 K	68.578 (1)	68.546 (1)	0	0.020 (2)
300 K	65.325 (1)	65.467 (1)	65.492 (1)	0	0.029 (2)	Und.†	200 K	68.704 (6)	68.676 (3)	0	0
350 K	65.370 (4)	65.517 (3)	65.549 (4)	0	0.012 (1)	Und.†	300 K	68.871 (4)	68.827 (3)	0	0
380 K	65.403 (1)	65.539 (6)	65.574 (4)	0	0	0	400 K	69.047 (6)	69.004 (3)	0	0
420 K	65.443 (2)	65.591 (7)	65.670 (2)	0	0	0					

† Biphasic samples, only the volume of the predominant phase is reported, whereas the related titanium displacement was not refined and it is reported as undefined (Und.).

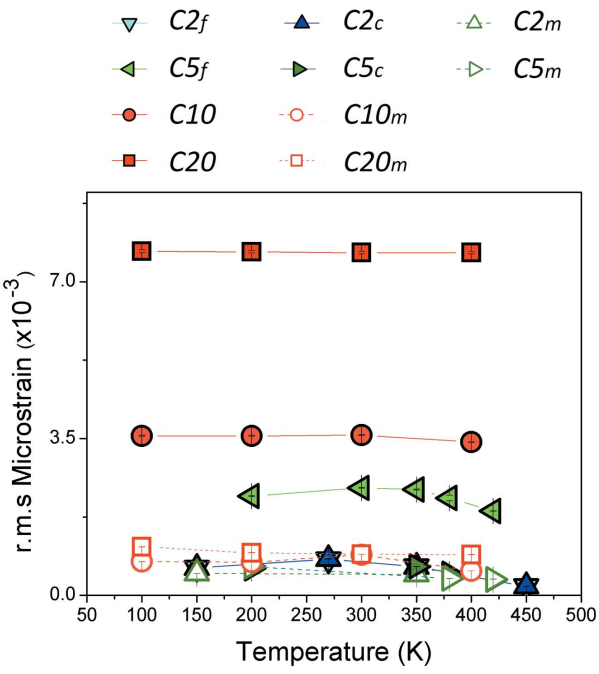

Figure 2
Comparison of r.m.s microstrain values in powder and micrometric (Confalonieri *et al.*, 2018) BCTs as a function of composition, temperature and particle size. Powder samples with high cerium amount show larger r.m.s microstrain values.

strain have to be investigated also on the local structure. With the aim of better understanding the nature of the average structural variations and exploring the origin of the size effect, PDF analysis was performed.

3.2. Pair distribution function refinements

3.2.1. Local structure. Different refinements were performed between 1 and 10 Å in order to determine the local symmetry, using the four space groups used in the refinement of the average structure. Resulting *Rw* values were compared, identifying the structure which gives the best fit. A supercell 2 × 2 × 2 was used to explore more realistic models for the local disorder, involving in particular Ti and Ce, which were constrained by fractional occupancies, but with independent (and refinable) positions. The isotropic thermal parameters and the atomic coordinates were refined together with the cell parameters. According to the *Rw* values, the tetragonal crystal system describes the local PDFs better. As an example, the refinements performed on the local structure at the lowest temperatures and for each composition and particle size are shown in Fig. 3. Table 4 reports the resulting local cell parameters and the related distortion, calculated as $t = 100[(c/a) - 1]$ (Rabuffetti *et al.*, 2014). This parameter, named tetragonality, shows a direct correlation with cerium amount: highest values belong to C20, whereas $C2_c$ and $C2_f$ present significant lower distortion. The relationship between composition (x), local distortion and material properties has already been recognized in micrometric BCTs. Confalonieri *et al.* (2018) report that cerium introduction induces increasing local distortion, which, in turn, decreases the titanium displacement correlation and then the average spontaneous polarization. For the sake of comparison, the local titanium displacement was also calculated (from the centre of the local cell) for the present powders. Likewise micrometric samples (Confalonieri *et al.*, 2018), Ti local displacements decrease as cerium concentration and local distortion increase (Table 5) due to their negative influence on dipole correlation. We can also observe that the displacements obtained for the powders are generally smaller than those of the micrometric ceramics.

3.2.2. Structural coherence and its correlation length. In order to evaluate the structure–properties relationship, it is crucial to understand how the local and the average structure are related: this is usually done by looking at the structural coherent correlation length. This can be evaluated by analysing and comparing the structure at different scales (*i.e* different radius ranges of the PDF). A perfect crystal is structurally coherent in the sense that all unit cells are precisely arranged in a 3D lattice and the atomic arrangement within each cell is identical (Fletcher, 1979). This means that, for example, local, medium and average structures are exactly superimposable. They are a perfect picture of the arrangement at the atomic level and the structural coherent correlation length is infinite. This is not true if single unit cells are affected by disorder. In this case, the local PDF represents an average of the correlations of all atomic variations of every single cell (Egami & Billinge, 2012). In turn, the medium structure derives from the correlation of the local variations and in the same way the average structure results from the averaging of

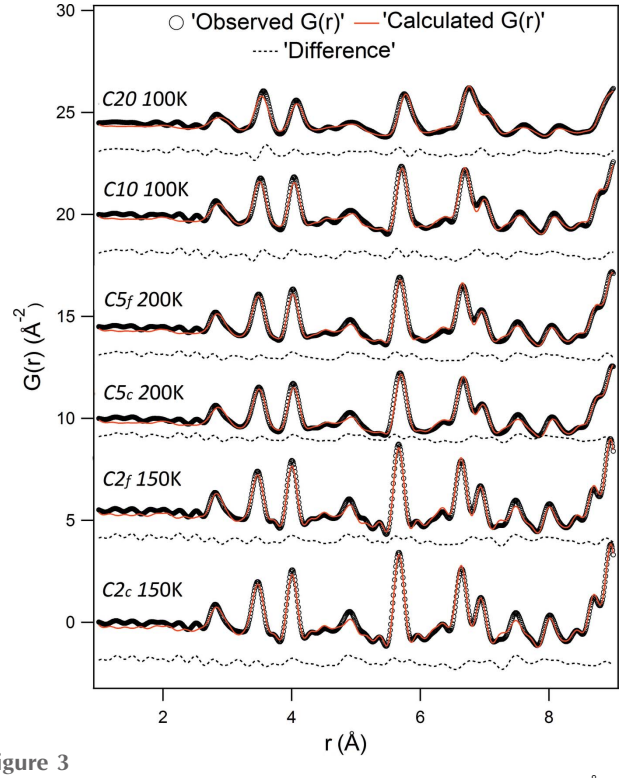

Figure 3
Example of local structural fits performed between 1 and 10 Å as a function of composition and particle size.

Table 4
Local cell parameters and the tetragonality, obtained in each of the three radius ranges.

	Local cell parameters (Å)			Tetragonality				Local cell parameters (Å)			Tetragonality		
Sample	1–10 (Å)	10–19 (Å)	19–28 (Å)	1–10 (Å)	10–19 (Å)	19–28 (Å)	Sample	1–10 (Å)	10–19 (Å)	19–28 (Å)	1–10 (Å)	10–19 (Å)	19–28 (Å)
$C2_f$							$C2_c$						
150 K	3.995	3.998	4.001	0.855	0.677	0.508	150 K	3.999	4.006	4.008	0.712	0.275	0.113
	4.029	4.026	4.021					4.028	4.017	4.013			
270 K	3.995	4.002	4.003	1.140	0.716	0.632	270 K	3.998	4.006	4.005	1.005	0.487	0.548
	4.040	4.031	4.028					4.038	4.026	4.027			
350 K	4.003	4.003	4.004	0.641	0.675	0.546	350 K	4.008	4.006	4.009	0.429	0.592	0.372
	4.029	4.030	4.026					4.025	4.030	4.024			
450 K	3.999	4.006	4.009	1.062	0.681	0.434	450 K	4.001	4.014	4.015	1.140	0.234	0.152
	4.042	4.033	4.026					4.047	4.023	4.021			
$C5_f$							$C5_c$						
200 K	4.008	4.021	4.017	0.990	0.195	0.505	200 K	4.012	4.023	4.024	0.870	0.215	0.124
	4.047	4.028	4.037					4.047	4.031	4.029			
300 K	4.008	4.017	4.020	1.250	0.723	0.556	300 K	4.019	4.024	4.024	0.544	0.274	0.236
	4.058	4.046	4.042					4.041	4.035	4.034			
350 K	4.012	4.020	4.021	1.106	0.671	0.501	350 K	4.024	4.025	4.026	0.251	0.245	0.137
	4.056	4.047	4.042					4.034	4.035	4.031			
380 K	4.013	4.019	4.021	1.081	0.805	0.621	380 K	4.017	4.026	4.024	0.739	0.222	0.307
	4.056	4.051	4.046					4.047	4.035	4.037			
420 K	4.019	4.026	4.024	0.719	0.343	0.400	420 K	4.025	4.028	4.028	0.257	0.087	0.044
	4.048	4.040	4.040					4.035	4.032	4.030			
C10							C20						
100 K	4.026	4.042	4.037	1.217	0.376	0.757	100 K	4.058	4.065	4.085	1.775	1.518	0
	4.075	4.057	4.068					4.130	4.127				
200 K	4.028	4.036	4.040	1.340	1.037	0.668	200 K	4.061	4.069	4.088	1.747	1.380	0
	4.082	4.077	4.067					4.132	4.125				
300 K	4.034	4.041	4.045	1.038	0.711	0.381	300 K	4.064	4.072	4.090	1.95	1.408	0
	4.076	4.070	4.060					4.143	4.129				
400 K	4.033	4.041	4.046	1.467	0.961	0.509	400 K	4.068	4.073	4.094	1.808	1.589	0
	4.092	4.080	4.066					4.142	4.137				

Table 5
Local titanium displacements of powders and micrometric ceramics (Confalonieri *et al.*, 2018) of the same composition.

	Ti site local displacement (Å)				Ti site local displacement (Å)	
Sample	Fine powder	Coarse powder	Micrometric ceramic	Sample	Powder	Micrometric ceramic
x = 0.02				x = 0.10		
150 K	0.020 (1)	0.023 (6)	0.056 (1)	100 K	0.017 (3)	0.034 (5)
270 K	0.018 (2)	0.017 (8)	0.067 (3)	200 K	0.016 (1)	0.052 (5)
350 K	0.022 (1)	0.020 (2)	0.057 (2)	300 K	0.016 (1)	0.045 (7)
450 K	0.012 (4)	0.013 (3)	0.062 (2)	400 K	0.015 (5)	0.057 (7)
x = 0.05				x = 0.20		
200 K	0.021 (4)	0.020 (2)	0.049 (4)	100 K	0.008 (3)	0.01 (3)
300 K	0.016 (3)	0.010 (3)	0.062 (3)	200 K	0.011 (3)	0.01 (2)
350 K	0.012 (4)	0.018 (1)	0.064 (3)	300 K	0.011 (1)	0.008 (5)
380 K	0.014 (1)	0.015 (1)	0.065 (6)	400 K	0.011 (4)	0.01 (2)
420 K	0.014 (1)	0.017 (6)	0.050 (9)			

the variations at the medium scale. Obviously, structures at different scales (*e.g.* local, medium, average) are not equivalent and the coherent correlation length is limited.

BCT's structural coherent correlation length was determined using a carbox approach, analyzing local structure in different PDF radius ranges, hence at different scales. Refinements, with the same strategy used in the range 1–10 Å, were also performed between ∼10 and ∼19 Å and ∼19 and ∼28 Å. Exact limits of these ranges were chosen *ad hoc* for each sample to not include partial or incomplete peaks in refinements. Comparing *Rw* values, tetragonal symmetry was appointed for all the sets and in each range. The only exception is C20 where, at all the temperatures, structure in the range 19–28 Å is significantly better described by cubic symmetry. Fig. 4 presents an example of carbox fits for C20 and C10 at 100 K. The value of tetragonality (t) can be calculated in each radius range (Table 4). In general, a decrease of t with increasing distance is observed, indicating a progressive weakening of the ferroelectric distortion. This tendency can be quantified by the slope of the regression line through the experimental points, that can be considered as an index of the structural correlation length. The larger the slope (absolute value), the smaller the structural coherent correlation length. Indeed, a large slope indicates that the tetragonality changes very fast with the radius. Fig. 5 displays the average value s of the slopes over different temperatures for each sample and its estimated standard deviation. All obtained values are negative, meaning that distortion decreases as the radius increases, irrespective of temperature. Moreover, the absolute value of s is practically constant for x = 0.02 and 0.05, and then increases

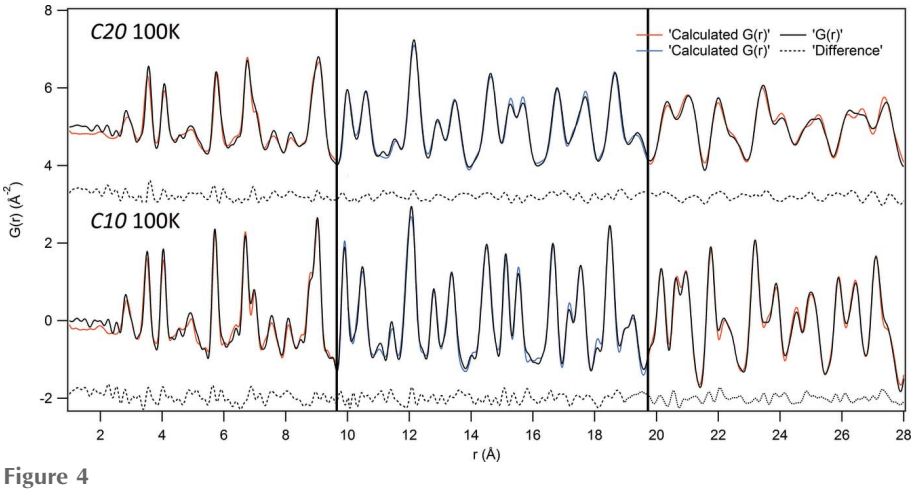

Figure 4
Example of Pair Distribution Function analysis performed in three consecutive radius ranges (carbox approach). Tetragonal structure was used in all the refinements except between ~19 and 28 Å for C20, where the symmetry was cubic.

with increasing cerium amount. Indeed, we can see from Table 4 that samples with larger cerium content (C10 and C20) are affected by a larger local distortion, which decreases quickly down to the smallest value in the third *r*-range. This indicates a short structural coherent correlation length, which reaches its minimum in sample C20 (Fig. 5). Thus, a higher amount of cerium determines a large local distortion which rapidly averages out with increasing *r* with the result that, on average, the cubic structure stability field is enlarged. The coupling of the effect of size and the amount of cerium acts as follows:

(i) High cerium amount (x = 0.10 and 0.20): despite particle size being in the submicrometre range, the samples with a high cerium content have an average cubic symmetry.

(ii) Intermediate cerium amount (x = 0.05): the reduction of particle size plays a dominant role. Samples $C5_c$ behaves in exactly the same way as its corresponding microcrystalline ceramics, while samples $C5_f$ can be assimilated to the samples with a larger cerium content (C10 and C20).

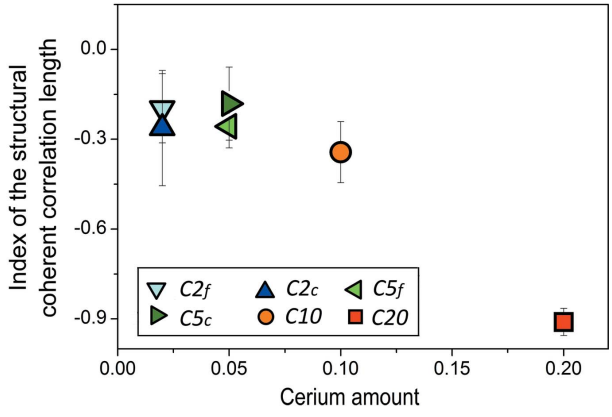

Figure 5
Slopes of the regression lines calculated from the tetragonality values obtained in different radius ranges. Slopes can be interpreted as an index of the coherent structural correlation length, which, as shown, decreases as a function of cerium amount.

(iii) Low cerium amount (x = 0.02): despite the reduced size, both samples behave as typical ferroelectric $BaTiO_3$ as a function of temperature.

3.2.3. Comparison between cerium substitution and its coupling with reduced particle size. The foregoing results indicate that both the incorporation of the foreign cation and the reduction of the particles size contribute to depress the average ferroelectric distortion of the lattice. Both, indeed, play an important role at the atomic level inducing local disorder and, in turn, influencing the structural coherent correlation length.

Cerium introduction in ceramic BCTs creates local distortions at the atomic level, due to the different size of cerium and titanium. The local structure in micrometric BCT ceramics, indeed, reveals a high disorder, which can be fitted only by a complex model (Confalonieri *et al.*, 2018). As a function of cerium amount, the local distortion increases (*i.e.* rhombohedral cell angle), in contrast to what happens to the structural coherent correlation length. For example, in micrometric BCTs with large Ce amount (*i.e.* x = 0.30) (Confalonieri *et al.*, 2018), the high local disorder affects the long-range correlations between polyhedra, even at low temperature, and the resulting average structure is always cubic. On the other hand, the ceramic sample with x = 0.02 shows a small local distortion and hence the coherent structural correlation length is rather long: the phase transitions, on the average structure, are the same as in the pure $BaTiO_3$.

When cerium introduction is coupled with the reduced size, the described effects are intensified. There are many signals of the atomic disorder: the first Ti—O/Ce—O peak is so broad and weak that, even by going at very high Q (and thus minimizing the termination ripples), it may not be possible to clearly see it (Fig. 3). Local tetragonality increases as a function of cerium concentration. Broadening of PDF peaks increases despite the symmetry increase (as occurs for C20 in the range 19–28 Å; Fig. 4). Despite these indications of disorder, the local symmetry is tetragonal, instead of rhombohedral as in the corresponding micrometric BCT. This may appear a difficult interpretation, but it should be borne in mind that, in samples with reduced size, the differences between single unit cells may be more widely distributed than in their micrometric counterpart. Therefore, their correlation length is strongly reduced and, even in the very local range (below 10 Å), they show a tetragonal symmetry. Moreover, the larger the tetragonality at the local level, the wider is the cubic structure stability field on average.

The reduction of particle size and the B site homovalent substitution therefore act together, decreasing the structural coherent correlation length. This increases, on average, the cubic phase stability suppressing the ferroelectric properties. According to the observations already made for pure $BaTiO_3$

(Petkov *et al.*, 2008; Smith *et al.*, 2008), the local structural disorder, regardless of its origins, plays a crucial role on the ferroelectric properties.

4. Summary and conclusions

The relationship between the effects of reduced size and amount of cerium content on the structure of $BaCe_xTi_{1-x}O_3$ powders was studied in detail, locally as well as at longer range.

The stability of the ferroelectric phases in $BaCe_xTi_{1-x}O_3$ was demonstrated to be strictly correlated to both the amount of cerium in the structure and the particle size. The two effects cooperate in the extension of the cubic structure stability field in comparison with the respective micrometric materials.

The results of this paper can be summarized as follows:

(i) The samples with $x = 0.02$ behave in the same way as the micrometric ceramics, regardless of their particle size. The reduced particle size at 80–160 nm and the very small amount of cerium in the structure do not produce, collectively, enough distortion in the local structure to determine a 'size effect' influencing the behaviour of the material.

(ii) The size effect can be seen in samples with $x = 0.05$, because the coarse powder behaves, as a function of temperature, in the same way as the micrometric ceramics with the same composition, while the fine powder (150–400 nm) suffers from the size effect, and it is cubic at all temperatures.

(iii) The effect of the amount of cerium can be seen in the samples with $x = 0.10$ and 0.20, where ferroelectric phases are no longer stable at any temperature even though the contribution of the reduced grain size is small, being well above 300 nm.

Our results therefore confirm that the local disorder of the structure is at the basis of the weakening or suppression of the ferroelectric order in a typical ferroelectric perovskite such as $BaTiO_3$ whether they originate from the incorporation of foreign ions or/and the reduction of particle/grain size.

Acknowledgements

The authors thank Dr Pavol Juhas (Brookhaven National Laboratory, Upton, NY, USA) and Dr Michela Brunelli (ESRF, Grenoble, France) for their help, and the staff of ID22 beamline (ESRF, Grenoble, France) for the support in data collection during experiments MA3151 and MA2497.

References

Alguero, M., Gregg, J. & Mitoseriu, L. (2016). *Nanoscale Ferroelectrics and Multiferroics Key Processing and Characterization Issues, and Multifferroics Key Processing and Characterization Issues and Nanoscale Effects.* New York: John Wiley and Sons.

Balzar, D., Audebrand, N., Daymond, M. R., Fitch, A., Hewat, A., Langford, J. I., Le Bail, A., Louër, D., Masson, O., McCowan, C. N., Popa, N. C., Stephens, P. W. & Toby, B. H. (2004). *J. Appl. Cryst.* **37**, 911–924.

Billinge, S. J. L. & Kanatzidis, M. G. (2004). *Chem. Commun.* pp. 749–760.

Canu, G., Confalonieri, G., Deluca, M., Curecheriu, L., Buscaglia, M. T., Asandulesa, M., Horchidan, N., Dapiaggi, M., Mitoseriu, L. & Buscaglia, V. (2018). *Acta Mater.* **152**, 258–268.

Cochran, W. (1960). *Adv. Phys.* **9**, 387–423.

Comès, R., Lambert, M. & Guinier, A. (1970). *Acta Cryst.* A**26**, 244–254.

Confalonieri, G., Buscaglia, V., Capitani, G., Canu, G., Rotiroti, N., Bernasconi, A., Pavese, A. & Dapiaggi, M. (2018). *J. Appl. Cryst.* **51**, 1283–1294.

Confalonieri, G., Dapiaggi, M., Sommariva, M., Gateshki, M., Fitch, A. N. & Bernasconi, A. (2015). *Powder Diffr.* **30**, S65–S69.

Curecheriu, L. P., Ciomaga, C. E., Musteata, V., Canu, G., Buscaglia, V. & Mitoseriu, L. (2016). *Ceram. Int.* **42**, 11085–11092.

Curecheriu, L. P., Deluca, M., Mocanu, Z. V., Pop, M. V., Nica, V., Horchidan, N., Buscaglia, M. T., Buscaglia, V., van Bael, M., Hardy, A. & Mitoseriu, L. (2013). *Phase Transit.* **86**, 703–714.

Egami, T. & Billinge, S. J. L. (2012). *Underneath the Bragg Peaks: Structural Analysis of Complex Materials*, Vol. 16, 2nd ed., pp. 1–481.

Farrow, C. L., Juhas, P., Liu, J. W., Bryndin, D., Bozin, E. S., Bloch, J., Proffen, T. & Billinge, S. J. L. (2007). *J. Phys. Condens. Matter*, **19**, 335219.

Fitch, A. N. (2004). *J. Res. Natl Inst. Stand. Technol.* **109**, 133–142.

Fletcher, N. H. (1979). *Physics of Materials*, edited by D. W. Borland, L. M. Clarebrough and A. J. W. Moore, pp. 63–72. Melbourne: CSIRO and University of Melbourne.

Frenkel, A. I., Frey, M. H. & Payne, D. A. (1999). *J. Synchrotron Rad.* **6**, 515–517.

Gerra, G., Tagantsev, A. K., Setter, N. & Parlinski, K. (2006). *Phys. Rev. Lett.* **96**, 107603.

Ihlefeld, J. F., Harris, D. T., Keech, R., Jones, J. L., Maria, J. P. & Trolier-McKinstry, S. (2016). *J. Am. Ceram. Soc.* **99**, 2537–2557.

Juhás, P., Davis, T., Farrow, C. L. & Billinge, S. J. L. (2013). *J. Appl. Cryst.* **46**, 560–566.

Kwei, G. H., Lawson, A. C., Billinge, S. J. L. & Cheong, S. W. (1993). *J. Phys. Chem.* **97**, 2368–2377.

Lin, S., Lu, T., Jin, C. Q. & Wang, X. H. (2006). *Phys. Rev. B*, **74**, 134115.

Lutterotti, L., Matthies, S. & Wenk, H. (1999). *IUCr: Newsletter of the CPD*, **21**, 14–15.

Miura, K., Azuma, M. & Funakubo, H. (2011). *Materials*, **4**, 260–273.

Moulson, A. & Herbert, J. (2003). *Electroceramics: Materials, Properties, Applications*, 2nd ed. New York: John Wiley and Sons.

Müller, K. & Berlinger, W. (1986). *Phys. Rev. B*, **34**, 6130–6136.

Müller, K., Berlinger, W., Blazey, K. & Albers, J. (1987). *Solid State Commun.* **61**, 21–25.

Nuraje, N. & Su, K. (2013). *Nanoscale*, **5**, 8752–8780.

Page, K., Proffen, T., Niederberger, M. & Seshadri, R. (2010). *Chem. Mater.* **22**, 4386–4391.

Petkov, V., Buscaglia, V., Buscaglia, M. T., Zhao, Z. & Ren, Y. (2008). *Phys. Rev. B*, **78**, 054107.

Rabuffetti, F. A., Culver, S. P., Lee, J. S. & Brutchey, R. L. (2014). *Nanoscale*, **6**, 2909–2914.

Shrout, T. R. & Zhang, S. J. (2007). *J. Electroceram.* **19**, 111–124.

Shvartsman, V. V. & Lupascu, D. C. (2012). *J. Am. Ceram. Soc.* **95**, 1–26.

Smith, M. B., Page, K., Siegrist, T., Redmond, P. L., Walter, E. C., Seshadri, R., Brus, L. E. & Steigerwald, M. L. (2008). *J. Am. Chem. Soc.* **130**, 6955–6963.

Yasmm, S., Choudhury, S., Hakim, M. A., Bhuiyan, A. H. & Rahman, M. J. (2011). *J. Mater. Sci. Technol.* **27**, 759–763.

Yoneda, Y., Kohara, S. & Kato, K. (2013). *Jpn. J. Appl. Phys.* **52**, 09KF01.

Zhu, X. & Liu, Z. (2011). *J. Adv. Dielect.* **01**, 289–301.